AUTOASSOCIATIVE LEARNING OF STRUCTURAL REPRESENTATIONS FOR MODELING AND CLASSIFICATION IN MEDICAL IMAGING

A PREPRINT

Zuzanna Buchnajzer

Kacper Dobek
 Stanisław Hapke
 Krzysztof Krawiec*
 Institute of Computing Science

Daniel Jankowski

Institute of Computing Science
Poznan University of Technology, Poznan, Poland
krawiec@cs.put.poznan.pl

November 26, 2024

ABSTRACT

Deep learning architectures based on convolutional neural networks tend to rely on continuous, smooth features. While this characteristics provides significant robustness and proves useful in many real-world tasks, it is strikingly incompatible with the physical characteristic of the world, which, at the scale in which humans operate, comprises crisp objects, typically representing well-defined categories. This study proposes a class of neurosymbolic systems that learn by reconstructing the observed images in terms of visual primitives and are thus forced to form high-level, structural explanations of them. When applied to the task of diagnosing abnormalities in histological imaging, the method proved superior to a conventional deep learning architecture in terms of classification accuracy, while being more transparent.

Keywords Representation Learning · Learning by Autoassociation · Neurosymbolic Systems · Differentiable Rendering

1 Introduction

Annotation of medical imaging is notoriously time-consuming, prone to human biases, and hard to reconcile with the insatiable demands of contemporary machine learning. Deep Learning (DL) models trained on annotated data are often narrow in focusing on features that are specific to a given context (anomaly, pathology, etc.) rather than discovering and capturing general characteristics of observed structures and processes, which may make them susceptible to deceptive image features and lead to inferior generalization.

We posit that one of the primary causes of this challenge is the unstructured character of DL architectures. Contemporary DL models are essentially intertwined compositions of dot products and nonlinearities, conglomerates of often billions of unsophisticated units that process data in a highly distributed and continuous, non-symbolic fashion. Their training requires large volumes of data, which are often hard to come by, and involves exorbitant amounts of compute and energy. If the task is posed within the supervised learning paradigm, those data need to be not only curated, but also annotated (labeled), which limits their availability even further. Last but not least, as each processing unit takes care only of a minuscule fraction of inference, it is very hard to explain the model and its decisions to a human in a transparent and succinct fashion.

In this study, we argue for stronger involvement of unlabeled data in the construction of analytic and diagnostic ML models and propose ASR, a neurosymbolic architecture trained to form Auto-associative Structural Representations, in which a generative decoder synthesizes physically plausible structural models that explain the observed image. ASR combines a convolutional encoder queried on a raster image with a symbolic decoder that performs differentiable

^{*}https://ml.cs.put.poznan.pl/en

rendering to reproduce that image. As the involved symbolic components are differentiable, the entire architecture can be efficiently trained with conventional gradient-based algorithms. ASR can learn effectively from relatively small data sets, offers better interpretability than conventional models, and promises better diagnostic accuracy.

2 The proposed method

2.1 Motivations

The blueprint of convolutional neural networks (convnets), the working horse of DL applications in computer vision (CV), assumes that aggregation of input pixels gives rise to higher-level features formed at consecutive layers, which are expected to convey information about (among others) structure and can be then used for inference. While this scheme proved very useful and effective in multiple contexts, its structural aspect is only *implicit* in the sense of depending on the interpretation of weights in units' receptive fields. In particular, convnets have no means of expressing the 'objectness' of their percepts. The entirety of processing is about manipulating *pixels*, whether these are literally the pixels available in the input image, or 'pixels' that embody higher-level features formed in further layers, usually at a lower spatial resolution.

The main motivation behind the proposed approach is to learn image interpretation in terms of representations that are *explicitly more structural and hierarchical* than in the mainstream DL, and in particular those learned by convnets. To this aim, we equip our model with the capacity of reasoning in terms of (relatively simple) *visual primitives*, rather than individual pixels. This representation is explicit and *enforced*, i.e. the model *has to* reason about the image in the prescribed terms.

To provide for the above enforcement, we resort to autoassociative learning: ASR is a neurosymbolic autoencoder that, given an input image, attempts to reproduce it with parameterized visual primitives. The reproduced image is compared to the input image using a reconstruction loss that is minimized with gradient in training.

We assume the visual primitives to be spatially continuous (so that they correspond to connected regions when rendered on rasters), compact, and tunable with parameters that allow the model to control their visual properties, like size, orientation, shape, and color (appearance). In this preliminary study, we resort to ellipses as a simple yet nontrivial class of primitives. We exemplify the approach by applying it to microscopic images of stained histological sections (Sec. 4); nevertheless, it can be generalized to other domains, including 3D volumetric imaging.

2.2 The architecture and training

The ASR autoencoder comprises three main components: an Encoder, a number of Modelers working in parallel, and a Renderer (corresponding to the decoder in conventional autoencoder architectures) (Fig. 1).

Encoder. The Encoder is a convnet implemented as a stack of ConvBlocks, each comprising a 2D convolutional layer, ReLU activation function, and batch normalization. Consecutive ConvBlocks have decreasing spatial dimensions (spatial scales) and an increasing number of output channels. The stack of ConvBlocks is concluded with a BackgroundBlock, which flattens the output of the last ConvBlock and maps it with a small dense network to three variables r_{bg} , g_{bg} , b_{bg} that are interpreted as the color components of background in later processing stages.

Modelers. In contrast to conventional autoencoders that process only the final output of the encoder, ASR makes use of multiple latents formed by ConvBlocks at several spatial scales. Let z_j denote the latent vector produced by the jth ConvBlock at a given location in the input image (the spatial grid). The task of the Modeler is to map z_j to human-interpretable parameters of the graphical primitive to be rendered by the Renderer.

There is a separate modeler for each spatial scale j (Fig. 1), realized as a trainable 1×1 convolution layer that maps z_j at each location in the image to six variables that control the rendering of the primitive at that location: the horizontal and vertical scaling factors $(w_j \text{ and } h_j)$, the rotation angle d_j , and the three RGB components a_j that control the primitive's color appearance. The layer features the sigmoid activation function to bound the output interval. Subsequently, w_j and h_j are linearly scaled to [0.1, 2], so that it becomes impossible to 'collapse' the primitive to a point, while the upper bound of 2 allows partial overlap of primitives. d_j is scaled to $[0, 2\pi]$.

As argued later, the quality of reproduction that guides the training process of ASR is only a means to the end of *learning informative structural representations*. Therefore, the absolute values of that metric are not very relevant. For this reason, and to avoid excessive computational cost, we resort to *spatially sparse rendering* of visual primitives, rather than allowing them to be 'anchored' at any pixel in the image. We achieve this with two means. Firstly, as in many convnets, the dimensions of the spatial latent decrease with scale, so that the receptive fields of individual elements of those latents, expressed in terms of the input image, become larger with consecutive scales. Secondly, each

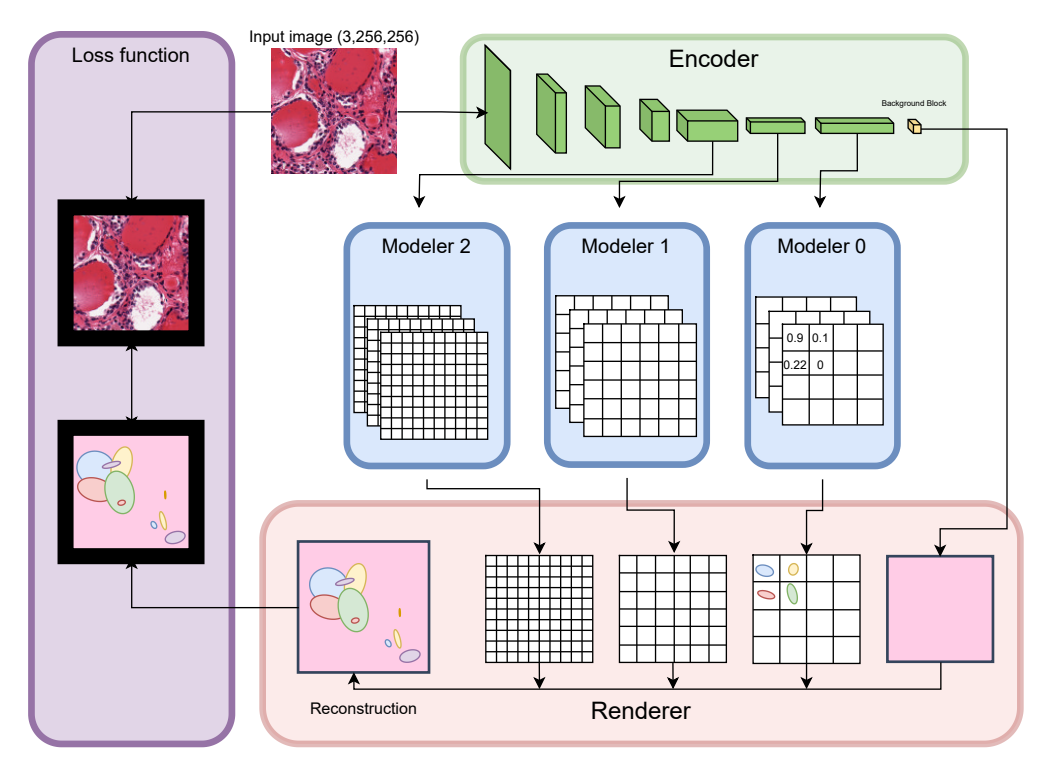


Figure 1: The overview of ASR's architecture.

Modeler is applied to its spatial latent with a stride greater than 1. As a result, the primitives at scale j are produced at certain spacing r_j and overlap only when the scaling factors w_j and h_j are relatively high. Technically, we set r_j to half the size of the receptive field at scale j.

In particular, we will show in Sec. 4 that such a representation, though not very precise at reproduction, is very informative for solving a concrete classification task.

Renderer. The Renderer produces the output image based on the parameters received from the Modeler. This involves three stages: rendering of individual primitives at scale j, combining them into a single resultant canvas at scale j, and merging these canvases into the final reproduction.

As ASR is meant to be trained end-to-end with gradient, the rendering process must be differentiable. While prior work on differentiable rendering exists (see, e.g., [Ravi et al., 2020, Li et al., 2020, Fuji Tsang et al., 2022, Jakob et al., 2022]), the elliptical shapes of our primitives allow achieving this goal with a relatively crude rendering of a blurry 'blobs' rather than 'crisp' ellipses. We realize this for a single primitive ellipse at a given location at scale j with the following steps:

- 1. Create a monochrome (single-channel) raster R_j of size $(2r_j + 1) \times (2r_j + 1)$.
- 2. Draw a centered blurry circle with radius r_j by setting the brightness of each pixel $p \in R_j$ to $\sigma(\beta(r_j d(p)))$, where d(p) is the distance of p from the center of R_j , σ is the sigmoid function, and β is the fuzziness coefficient that controls the sharpness of the contour.
- 3. Construct the affine transformation matrix A based on the scaling coefficients (w_j, h_j) and rotation d_j predicted by the Modeler.
- 4. Apply A to R_j : generate a transformed grid from A and use it to sample from R with bilinear interpolation (so this step is differentiable too).
- 5. Multiply R_i by the appearance descriptor a_i to produce an RGB image of the same dimensions.

Notice that the resulting R is approximately double the size of the grid cell, which allows the rendered primitives to overlap if necessary, as signaled earlier.

The R_j s for all grid cells are subsequently fused into a single canvas that represents the rendering outcome at the jth scale. To this aim, the individual Rs are spatially co-registered, i.e. placed at grid cells in the coordinate system of the

canvas, and their pixel values are aggregated. As in this study, we are interested in imaging in transmissive mode, where the light is absorbed by objects (rather than reflected or emitted by them), we perform multiplicative aggregation of the complements of Rs in each RGB channel independently, so that the resultant channel value of a pixel (x, y) in the canvas is $\Pi_i(1-R_i^{(i)}(x,y))$ where $R_i^{(i)}(x,y)$ is the channel value of pixel (x,y) in ith raster at scale j, after spatial co-registration.²

The final reproduction is obtained by element-wise multiplication of the canvases obtained for particular scales j, followed by the multiplication with the background canvas, which is uniformly filled with the RGB values predicted by the BackgroundBlock.

It is worth noticing that the Renderer does not involve any trainable parameters, and therefore its only role in training is to back-propagate the feedback received from the reconstruction error (the loss function) to the preceding components of the architecture, viz. the Modeler and the Encoder.

In principle, the hyperparameters of ASR can be set arbitrarily. However, care should be taken when setting the grid spacing r_i . For the Modeler and the Renderer to be able to faithfully reproduce the input observed in a given part of the input image, the grid spacing at a given scale j should be similar to the size of the receptive field of units in the corresponding ConvBlock. If the receptive field is smaller than grid spacing, the Renderer will attempt to produce objects based on only partial information available in its visual field, which may destabilize the training process. Conversely, if the receptive field is too big relative to grid spacing, the Renderer can be 'frustrated' by being unable to render some large objects it observes.

Training. ASR is trained with gradient descent by minimizing the loss function defined as the mean square error between the reproduction produced by the Renderer and the input image, averaged over pixels and RGB channels. We ignore the image margin of width 16 pixels in this calculation, to lessen the impact of border effects (the model may be struggling to reproduce the structures located close to the borders, as they can be only partially visible, extending beyond the image). We refer to this cropped variant of MSE as Masked MSE (MMSE).

Preliminary experiments indicated the importance of parameter initialization, which is due to the unusual/nontrivial processing taking place in the Renderer and the presence of sigmoid functions in Modelers. Therefore, we initialize the weights of ConvBlocks and Modelers with the Xavier method [Glorot and Bengio, 2010], but sample their biases from N(0,1) and set the bias of the BackgroundBlock to 1 to encourage it to participate in the rendering process.

3 **Related work**

ASR represents the category of image understanding systems inspired by the "vision as inverse graphics" blueprint [Barrow et al., 1978], which can be seen as a computer vision instance of the broader analysis-by-synthesis paradigm. While considered in the CV community for decades (see, e.g., [Krawiec, 2007]), it experienced significant advancement in recent years, thanks to the rapid progress of DL that facilitated end-to-end learning of complex, multi-staged architectures. Below, we review selected representatives of this research thread; for a thorough review of other approaches to compositional scene representation via reconstruction, see [Yuan et al., 2023]; also, Elich et al. [2022] present a compact review of numerous works on related CV topics, including learning object geometry and multi-object scene representations, segmentation, and shape estimation.

The Multi-Object Network (MONet) proposed by Burgess et al. [2019] is a composite unsupervised architecture that combines image segmentation based on an attention mechanism (to delineate image components) with a variational autoencoder (VAE), for rendering individual components in the scene. As such, the approach does not involve geometric aspects of image formation and scene understanding. Also, it does not involve geometric rendering of objects: the subimages of individual components are generated with the VAE and 'inpainted' into the scene using raster masks.

PriSMONet by Elich et al. [2022] attempts decomposition of 3D scenes based on their 2D views. Similarly to MONet, it parses the scene sequentially, object by object, and learns to generate objects' views composed from several aspects: shape, textural appearance, and 3D extrinsics (position, orientation, and scale). The background is handled separately. Object shapes are represented using the Signed Distance Function formalism, well known in CV, and generated using a separate autoencoder submodel (DeepSDF); in this sense, PriSMONet does not involve shape priors. In contrast to [Burgess et al., 2019], the architecture engages differentiable rendering.

Another related research direction concerns part discovery, where the goal is to decompose the objects comprising the scene into constituents, which preferably should have well-defined semantics (i.e., segmentation at the part level, not

²As any given raster overlaps only with the neighboring rasters, this aggregation is limited to the neighborhood.

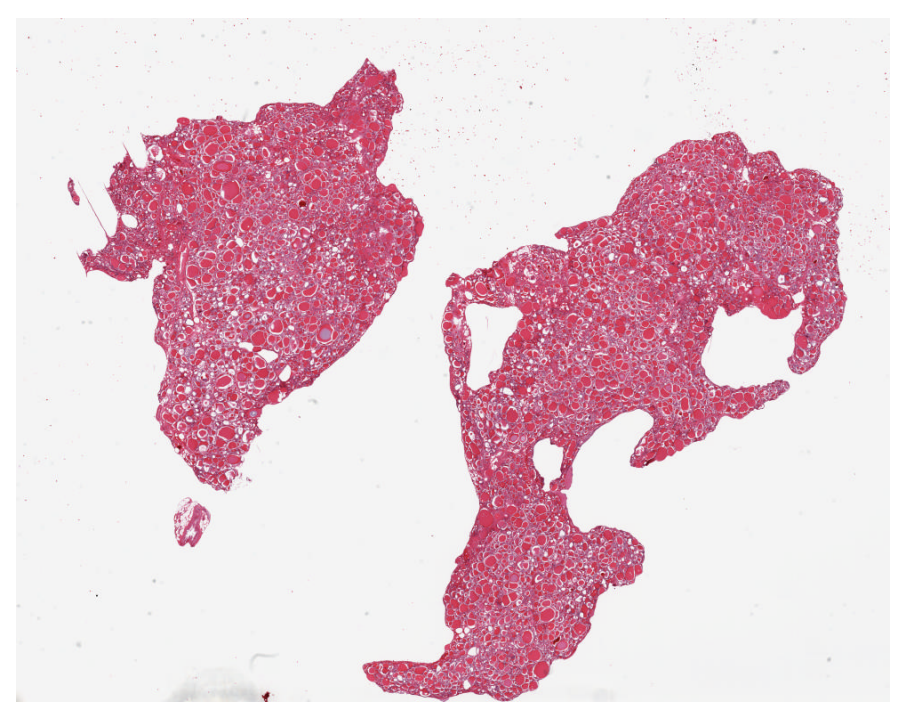


Figure 2: Example Thyroid Gland Whole Slide Image from the Biospecimen Research Database (BRD) Bio [2023]

the object level). The approaches proposed therein usually rely on mask-based representations (see, e.g. [Hung et al., 2019, Choudhury et al., 2021]); some of them involve also geometric transforms (e.g. [Hung et al., 2019]).

Krawiec and Nowinowski [2024] recently proposed a related neurosymbolic architecture that uses a domain-specific language to capture selected priors of image formation, including object shape (represented using elliptic Fourier transform), appearance, categorization, and geometric transforms. They express template programs in that language and learn their parameterization with features extracted from the scene by a convnet. When executed, the parameterized program produces geometric primitives which are rendered and assessed for correspondence with the scene content and trained via auto-association with gradient. The authors confront their approach with a baseline method on a synthetic benchmark and demonstrate its capacity to disentangle selected aspects of the image formation process, learn from small data, correct inference in the presence of noise, and out-of-sample generalization.

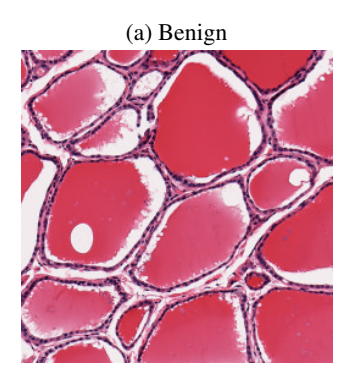
4 Experimental validation

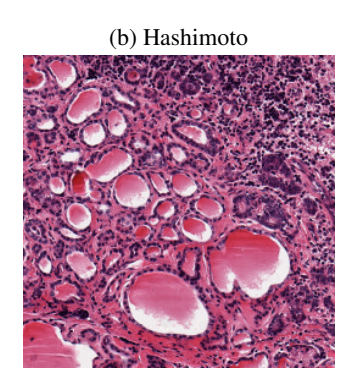
The experimental validation presented in the following comprises Stage 1 of representation learning (Sec. 4.4) and Stage 2 of learning to classify (Sec. 4.5). In the former, we train ASR and baseline models (all autoencoders) on a training set of images via autoassociation, to allow them to form informative latent representations. The primary objective in this stage is the quality of reconstruction. In Stage 2, we compose the encoders extracted from the models obtained in Stage 1 with decision trees to perform image classification. The main research question is whether the structure-aware representations formed by ASR in Stage 1 translate in Stage 2 to better test-set accuracy than the baseline models.

4.1 Problem statement and data

As the challenges outlined in the Introduction are particularly relevant for medical imaging, we focus on this realm. Given that ASR, as described in Sec. 2, is designed to reconstruct images specifically with elliptical shapes, we choose microscopic histological imaging, where cells and other structures can be expected to lend themselves to modeling with such primitives. More specifically, we consider images of the human thyroid as the subject of this study. Thyroid follicles filled with colloid hormones form the major mass of the organ, and are usually oval, or almost round; see examples in Figs.2 and 3. Yet they vary in shapes, sizes, orientations, colors, and spatial arrangements, which makes them a perfect yardstick for the kind of modeling implemented by ASR.

We rely on the Biospecimen Research Database [Bio, 2023] as the source of examinations for this study. This database is a large repository of digital slides containing, among others, 893 Whole Slide Images (WSIs) of the thyroid gland,





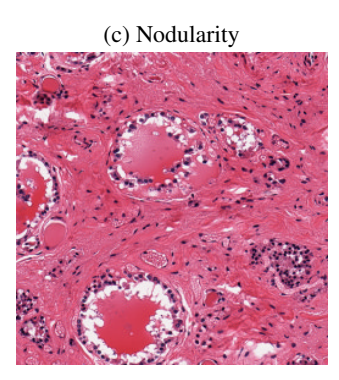
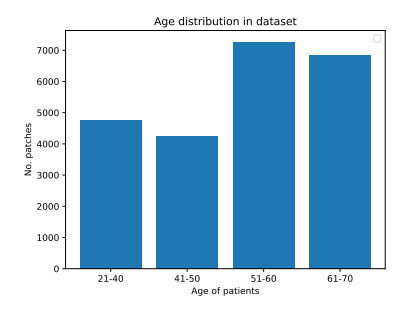
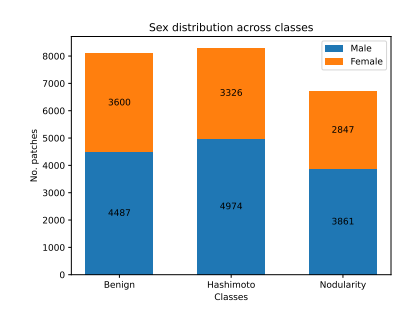


Figure 3: Examples of patches extracted from three different WSIs of the thyroid gland. In the Benign class (a) the follicles are regularly distributed across the tissue and have a circular shape. Aside from the vesicles, not much connective tissue is visible. The Hashimoto's disease (b) features lymphoplasmacytic infiltration, which manifests as numerous dark purple-stained cells (lymphocytes) in the interfollicular area, while the follicles are smaller and sparsely distributed. In Nodularity (c), we observe a small number of thyroid follicles and a high proportion of connective tissue.





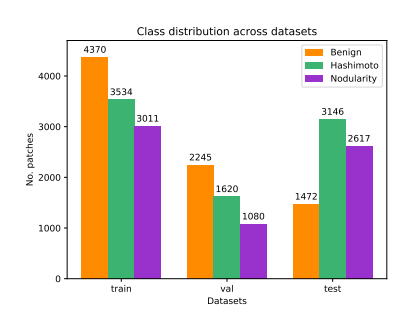


Figure 4: The distribution of age (left) and sex and decision class (center) in the generated set of image patches. The right inset presents the distribution of decision classes after dataset partitioning into training, validation, and test sets.

each at least $50k \times 50k$ pixels in size and typically covering a specimen of at least 10 by 10 mm (see example slide in Fig. 2). The slides are available in Aperio SVS format, which we parsed using the *slideio* library [Janowczyk, 2020] that allows reading in both image data and metadata.

From this collection, we selected a representative sample of 30 examinations representing three clinical conditions (decision classes): Benign (no abnormalities), Hashimoto, and Nodularity. When sampling, we provided balanced distributions of sex and age of patients (Table 3). The class assignment is based on the golden standard, as present in the clinical review comments included in the metadata. The selected sample is publicly available. Example fragments of the slides are shown in Figure 3. Though dimensions of images vary significantly in the sample, their spatial resolution is the same (0.4942 μ m/pix). The apparent magnification (AppMag) is also constant across the dataset (20).

We divide the 30 selected examinations into training set (15 examinations), validation set (6 examinations) and test set (9 examinations). This sampling was stratified, so that these proportions hold also in each decision class. Each examination comes from a different patient.

WSIs are too large to process them directly with DL models and, as exemplified in Fig. 2, usually contain a substantial fraction of white, uninformative background. Therefore, we extract patches from WSIs by scanning them systematically with a 1024×1024 sliding window at horizontal and vertical stride of 635 pixels (2/3 of window size) and accept only the patches that are occupied with tissue in at least 80%. Then, we downsize them to 256×256 pixels. This results in from 400 to $1550\ 256 \times 256$ patches per WSI. As a result, the train:validation:test proportions of 15:6:9 on the level of examinations translate to 10.915:4.945:7.235 on the level of image patches. As a side-effect, the distributions of decision classes in these subsets are not uniform and diverge significantly (Fig. 4).

 $^{^3}$ https://drive.google.com/file/d/1xpjTIJ1pB9KawD7AveaVTq770zpM8Ww0/view?usp=share_link

4.2 Configuration of ASR

We configure ASR so that its encoder comprises 3 ConvBlocks (Sec. 2.2), which implies that modeling and reconstruction take place at 3 scales/resolutions corresponding to those blocks: the highest (finest, j=2, grid spacing $r_2=128$), the intermediate ($j=1, r_1=64$), and the lowest (coarsest, $j=0, r_0=32$). The grid dimensions at those scales are, respectively, 2×2 cells, 4×4 cells, and 8×8 cells. This implies that the encoder parameterizes 84 ellipses in total. As each of them requires 6 parameters, the total dimensionality of the structural latent is 504.

All models are designed to process the downsized 256×256 patches. They were trained for up to the number of epochs indicated in the following, unless the PyTorch's EarlyStopping component signaled stagnation on the validation set (with patience of 20 epochs). For details on other common settings and elements of the configuration, see Section B.

4.3 Compared variants of the method

We compare three variants of ASR and one baseline configuration, detailed in the following.

Base. The base variant of the method, as presented in Sec. 2, trained with the MMSE reconstruction loss for up to 50 epochs.

Regularized. In preliminary experimenting, ASR exhibited a significant tendency to rely primarily on rendering at higher resolutions (on the denser grids), while neglecting the lowest resolutions. As this is at odds with our goal of learning succinct and transparent representations, we devise a regularization mechanism to curb the total number of graphical primitives used in rendering. We define the Appearance Regularization Value as:

$$ARV(\widehat{y}) = \frac{1}{|Loc_J|} \sum_{j \in J} \sum_{l \in Loc_j} w_j (a_l^j)^{\alpha}$$
(1)

where \hat{y} is the reconstruction image, J is the set of all scales, Loc_J is the set of variables describing shapes for all scales in \hat{y} , Loc_j is the set of variables describing shapes at scale j, w_j is the weight of scale j, a_l^j is the three-dimensional vector of RGB color components at scale j and location l, and α is the factorization parameter $\in (0.5, 1.0)$. Based on preliminary experimenting, we set the scale weights as follows: $w_0 = 0.6$, $w_1 = 0.9$, and $w_2 = 1.2$. The trade-off between this regularization term and the quality of reconstruction is controlled by weighing ARV in the total loss:

$$Loss(y, \widehat{y}) = MMSE(y, \widehat{y}) + \lambda_a ARV(\widehat{y}), \tag{2}$$

where we set λ_a to 0.009 in the course of preliminary tuning. Similarly to the Base configuration, Regularized models are trained for 50 epochs.

Incremental. While the models trained with regularization indeed turned out to use high-resolution rendering more sparingly than the base configurations, we sought other means of addressing their over-representation. We devised an incremental training procedure, in which the model is forced to rely more on the coarser resolutions earlier in training, while with time being gradually allowed to use the higher-resolution primitives. This is achieved by multiplying all outputs of the Modeler for scale j by β_j . We start with $\beta_0=1$ and $\beta_1=\beta_2=0.01$. Then, β_j s are increased after each epoch according to the formula:

$$\beta_i \leftarrow \min(1.0, \beta_i + \gamma_i).$$
 (3)

Based on preliminary experimenting, we set $\gamma_1 = \gamma_2 = 0.1$ and $\gamma_0 = 0$, i.e. the rendering at the lowest-resolution scale is unaffected by this mechanism and remains constant throughout training. Importantly, the above incrementing commences only in epoch 8 for scale 1 and in epoch 20 for scale 2.

The Incremental configuration engages also regularization described in the Regularized variant, albeit only from the 35th epoch, to avoid the potentially unstable interference of both mechanisms. Training lasts for up to 55 epochs, i.e. 5 epochs more than the previous variants, to give the regularization mechanism enough time to influence the model.

Baseline. As a baseline, we use a conventional convolutional autoencoder with a global latent. Its encoder starts with a stack of encoder blocks, each comprising a convolution layer, an Exponential Linear Unit (ELU) activation function, batch normalization, and a 2D max pooling layer. This is followed by flattening to a vector and a single dense layer that produces the global latent. We set the dimensionality of the global latent to 200 as a compromise between the computational cost and reconstruction quality. The decoder is a stack of decoder blocks, each comprising a 2D up-sampling layer with nearest neighbor interpolation, a convolution layer with ELU activation function, and batch normalization. As for ASR, the input and output are 256×256 RGB images. The architecture has 3,781,509 trainable parameters and has been trained for up to 50 epochs.

Table 1: The performance of individual runs of three variants of ASR and the Baseline autoencoder. Gray background
marks the model with the best MSE within a configuration.

MODEL	MAE ↓	MSE ↓	SSIM ↑	MMSE ↓
Base_1	0.1393	0.0342	0.1936	0.0342
Base_2	0.1370	0.0330	0.1943	0.0330
Base_3	0.1362	0.0327	0.1938	0.0326
Base_4	0.1367	0.0329	0.1924	0.0329
Base_5	0.1363	0.0326	0.1921	0.0325
Mean	0.1371	0.0331	0.1932	0.0330
Regularized_1	0.1415	0.0341	0.1968	0.0341
Regularized_2	0.1417	0.0341	0.1976	0.0341
Regularized_3	0.1431	0.0350	0.1972	0.0350
Regularized_4	0.1407	0.0342	0.1976	0.0342
Regularized_5	0.1412	0.0345	0.1961	0.0345
Mean	0.1416	0.0344	0.1971	0.0344
Incremental_1	0.1415	0.0342	0.1956	0.0342
Incremental_2	0.1424	0.0347	0.1958	0.0347
Incremental_3	0.1428	0.0349	0.1968	0.0349
Incremental_4	0.1466	0.0366	0.1961	0.0366
Incremental_5	0.1420	0.0346	0.1960	0.0346
Mean	0.1431	0.0350	0.1961	0.0350
Baseline_1	0.1178	0.0274	0.2299	-
Baseline_2	0.1187	0.0276	0.2271	-
Baseline_3	0.1179	0.0272	0.2295	-
Baseline_4	0.1174	0.0271	0.2292	-
Baseline_5	0.1202	0.0278	0.2227	-
Mean	0.1184	0.0274	0.2277	-

4.4 Stage 1: Image reconstruction

In this stage, we train all configurations on the image patches derived from the 15 training examinations, to perform image reconstruction, i.e. the diagnostic labels are ignored. For each configuration, we conduct 5 runs that start with a different initialization of the model's weights.

Table 1 compares the performance of configurations in terms of four reconstruction metrics comparing the produced output image to the input image, all calculated on the test set: Mean Absolute Error (MAE), Mean Square Error (MSE), Structural Similarity Index Measure (SSIM) by Wang et al. [2004], and Masked MSE (MMSE), i.e. the actual reconstruction loss used in training (Sec.2.2). For each configuration, five models have been trained, each starting from a different initialization.

The values of MMSE are systematically very close to those of MSE, which suggests that ASR copes well with border effects. Nevertheless, ASR configurations fare worse than the Baseline on all metrics. However, the differences are not large; for instance, on MAE, the best ASR configurations lag behind the mean Baseline by less than 0.02 (the maximum per-pixel MAE is 1). Among the ASR configurations, it is interesting to observe that both the Regularized and Incremental variants improve upon Base on SSIM while deteriorating on MAE and MSE. This suggests that they tend to pay more attention to the structures present in images, rather than individual pixels, which aligns with the motivations of this study. These observations are to some extent corroborated with the visual representation of reconstructions, shown in Fig. 5.

4.5 Stage 2: Classification

In this stage, we use the encoders of models trained in Stage 1 to obtain diagnostic models that classify the image patches into the three considered classes (Benign, Hashimoto, Nodularity).

Data preparation. To increase the number of examples available for training and evaluation of classifiers (compared to the bare 30 examinations), we conduct this experiment on bags of image patches. Each bag is a set of 16 patches drawn randomly (without replacement) from the same examination and inherits its decision class label. This results in 1,463 bags, with train:validation:test proportions of 694:312:457. Figure 6 presents the distribution of decision classes in those subsets which, unsurprisingly, follows the distribution shown in the rightmost inset in Fig. 4.

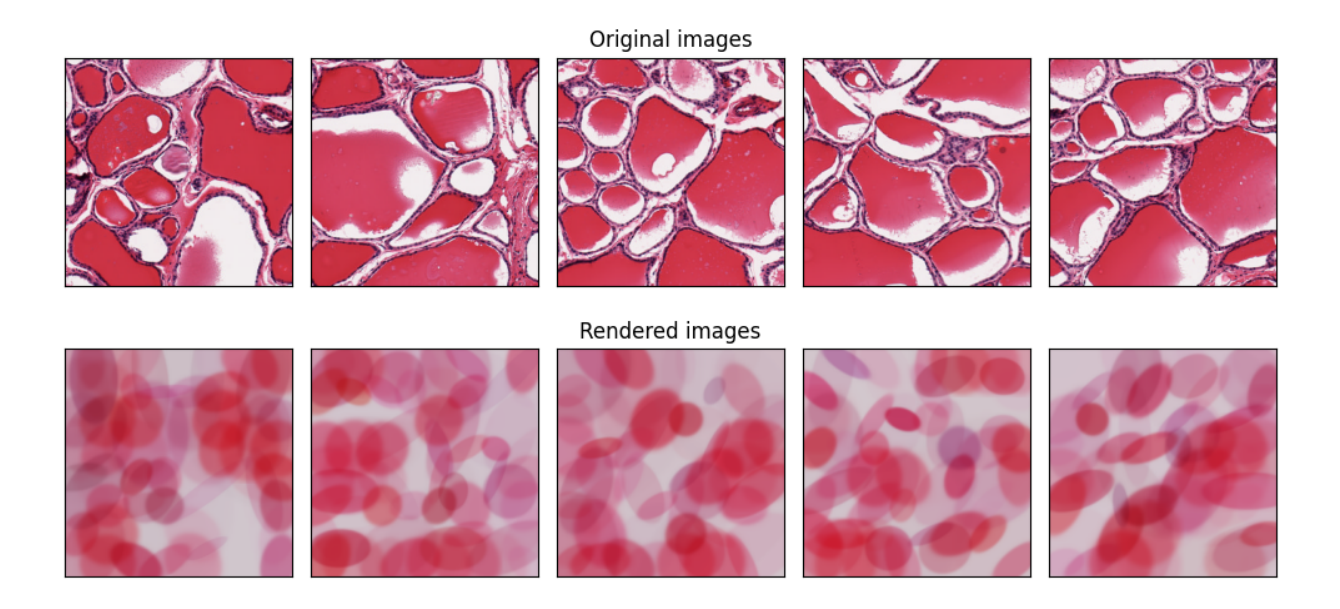


Figure 5: Reconstructions of sample test images produced by the REG_2 model.

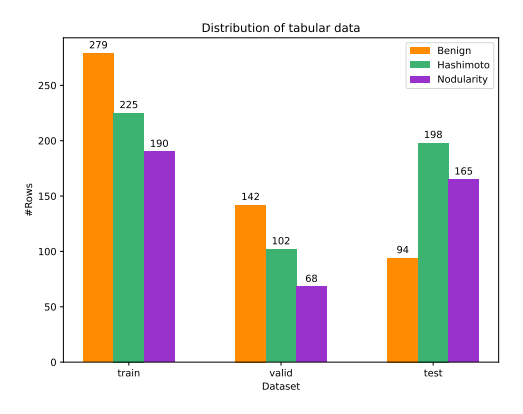


Figure 6: The distribution of classes in the tabular data is strongly correlated with the original distribution of the number of patches as shown in Figure 4.

The encoders produce image features that are subsequently used to train and test a classifier. For ASR, this process comprises the following steps for a given bag B:

- 1. Querying the Encoder and the Modelers on each of the sixteen 256×256 image patches from B, each resulting with vectors of latent features per scale and location in grids.
- 2. Aggregation of the latent features simultaneously over space (the X and Y dimensions of the spatial latent) and over *B*, for each scale (0, 1, 2) and each latent variable independently. For instance, one of such variables is the rotation of the ellipse at scale 0. As there are 6 ellipse-controlling variables at each scale, there are 18 variables in total. These are then aggregated independently using mean and standard deviation, resulting in 36 features.

The result of the above process is a tabular dataset of 1,463 bags (examples, rows) described by 36 attributes (columns) and partitioned into the three considered decision classes. The partitioning of that dataset into training, validation and test subsets is the same as in Sec. 4.1.

For the Baseline autoencoder, we proceed analogously: the encoder is queried on all image patches from B, and the resulting latent dimensions are aggregated over B. However, given the high dimensionality of this latent and its global

Table 2: Test-set predictive performance of each model. Gray shading marks the best model in terms of both accuracy and F1-score within a given group.

MODEL	accuracy ↑	precision ↑	recall ↑	f1_score ↑
Base_1	0.5864	0.6245	0.5864	0.5048
Base_2	0.7768	0.8096	0.7768	0.7735
Base_3	0.7112	0.7164	0.7112	0.7038
Base_4	0.5930	0.5907	0.5930	0.5523
Base_5	0.7615	0.7957	0.7615	0.7414
Regularized_1	0.6980	0.7044	0.6980	0.6738
Regularized_2	0.7133	0.7040	0.7133	0.7040
Regularized_3	0.6827	0.6762	0.6827	0.6655
Regularized_4	0.6674	0.7079	0.6674	0.6785
Regularized_5	0.7133	0.7245	0.7133	0.7075
Incremental_1	0.7090	0.7471	0.7090	0.6892
Incremental_2	0.6958	0.7058	0.6958	0.6998
Incremental_3	0.6521	0.7061	0.6521	0.6131
Incremental_4	0.7505	0.7568	0.7505	0.7511
Incremental_5	0.7396	0.7651	0.7396	0.7339
Baseline_1	0.4486	0.2979	0.4486	0.3572
Baseline_2	0.4311	0.3945	0.4311	0.3797
Baseline_3	0.2801	0.3729	0.2801	0.2342
Baseline_4	0.3129	0.3928	0.3129	0.2776
Baseline_5	0.5383	0.4108	0.5383	0.4486

character (it captures the entire 256×256 patch), we use only arithmetic mean for aggregation, applying it to each latent dimension independently. Therefore, for the Baseline, the resulting tabular dataset has dimensions 1,463 bags × 200 attributes (columns).

The induction algorithm. To demonstrate the explanatory potential of ASR, we choose decision trees as the predictive model to be trained on the tabular datasets prepared in the way described above. We use the DecisionTreeClassifier implementation from the scikit-learn library [Pedregosa et al., 2011] that relies on an optimized version of the CART algorithm [Breiman et al., 1984]. In training, we optimize the tree induction algorithm by exhaustively iterating over 30 following combinations of hyperparameter values: node impurity measure (gini, entropy), maximum height of the tree $(3, 4, 5, 7, \infty)$, and the minimum number of samples per leaf (5, 10, 20). For each of those combinations, the accuracy of classification is assessed using a 5-fold cross validation conducted on the training part of the tabular dataset. The combination that maximizes this measure is subsequently used to build a decision tree from the entire training set; however, to further maximize the predictive capability, this tree undergoes adaptive pruning using the minimal cost-complexity method. The intensity of pruning is controlled by the ccp alpha parameter of DecisionTreeClassifier, with 0 being a neutral value (no pruning) and larger values causing folding of terminal subtrees into leaves. We tune ccp alpha to maximize the classification accuracy on the validation set. The tree pruned in this way is subsequently tested on the test set.

Results. We produce a decision tree in the above way for each ASR and Baseline model listed in Table 1, and asses its predictive capacity on the testing part of the tabular dataset. Table 2 presents the accuracy of classification, precision, recall and F1 score of each of those classifiers. Notably, all configurations of ASR outperform the Baseline models on all metrics, and do so by a large margin. The best Baseline model is not better than the worst ASR model on any metric. One may argue that this may be due the Baseline models having over 5 times more attributes at their disposal (200 vs. 36). However, the extensive hyperparameter tuning provided fair footing for the Baseline configurations, allowing them to pick the optimal hyperparameter values and pruning intensity. Apparently, however, this was not sufficient for Baseline to perform well: the 'anonymous' features of its latent representation were not informative enough to provide for good predictive capacity. ASR, in contrast, managed to provide the decision trees with useful diagnostic information - even though at the time of Stage 1 training (Sec. 4.4) it was oblivious about decision classes.

Statistical analysis of the results presented in Table 2 ANOVA and post-hoc Holm test indicate statistically significant superiority of each variant of ASR compared to the Baseline, on accuracy of classification and on the F1 score (Sec. C). There are no significant differences between the variants of ASR. Notably, the Base variant exhibits most variance between runs, while the Regularized one is most stable in this respect.

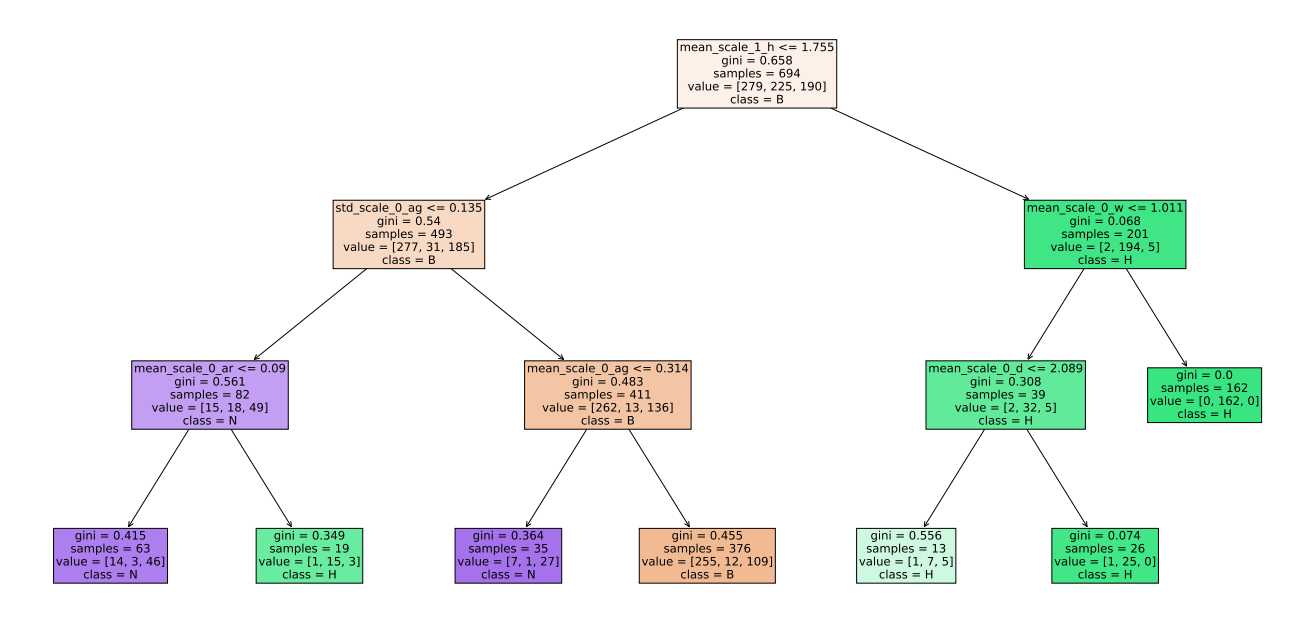


Figure 7: The final pruned decision tree induced from the attributes provided by the BASE_2 model.

Figure 7 presents the decision tree that achieved the best accuracy of classification across all ASR runs (the second run of the Base configuration). Similarly to other trees induced from the ASR-generated latent representation (not shown here for brevity), this tree nicely delineates most examples of the Hashimoto decision class (H) already at the root of the tree, using the mean of the height (h) ellipse parameter at scale j=1. The remaining two decision classes (N and B) turn out to be much harder to differentiate. Overall, the Nodularity class turns out to be hardest to classify, which we attribute to the relatively large fraction of connective tissue and sparse, small blobs, which are difficult to reconstruct using only ellipses (Fig. 3). Additionally, the examinations from this decision class occasionally feature inflammation, which can be mismatched with some visual features of Hashimoto.

More importantly, the obtained decision tree is notably small, comprising only 6 decision nodes and 7 leaves⁴. Other trees induced from attributes provided by ASR were similarly compact. This corroborates the main hypothesis of this study, i.e. that the structural, compositional representation enforced by ASR correlates better with relevant visual features, and provides a solid basis for successful classification. Interestingly, out of the five unique attributes used by decision nodes, only one (the one used by the root node) comes from scale j = 1, and none come from the scale j = 2. This signals that the features of large, coarse ellipses built at the lowest scale are most useful for this particular diagnostic scenario. To verify this supposition, we performed feature importance analysis by assessing the gain of the Gini criterion for each attribute (a.k.a. Gini importance), and averaged it over the final, optimized and pruned decision trees obtained in all 15 runs of ASR variants. Figure 8 shows the result of this analysis, which confirms that scale 0 features are most important, followed by scale 1 and then scale 2. In the group of color features (ar, ag, ab), the standard deviation of the green color component at scale 0 turns out to be particularly informative; this may be caused by the transmissive nature of the imaging process, in which changes in the green component result in different shades of purple. Among the geometric features, the standard deviation of the orientation angle of the ellipse (d) at the same scale proves most informative.

The above description demonstrates also the transparency of ASR, where decision-making process can be traced back to interpretable attributes expressed in terms of visual concepts that are intuitive for humans. Prospectively, this capability can be further exploited by, for instance, pointing to the geometric primitives (here: ellipses) that contributed most to particular stages of the decision-making process, represented by the individual nodes of the decision tree.

5 Conclusions

In this study, we provided preliminary evidence for the usefulness of a new representation learning approach, in which the learner is forced to 'explain' the data in terms of higher-level concepts available in the rendering process. This

⁴It is easy to notice that the pruning algorithm failed to fold the right-hand Hashimoto subtree, which would further reduce these numbers

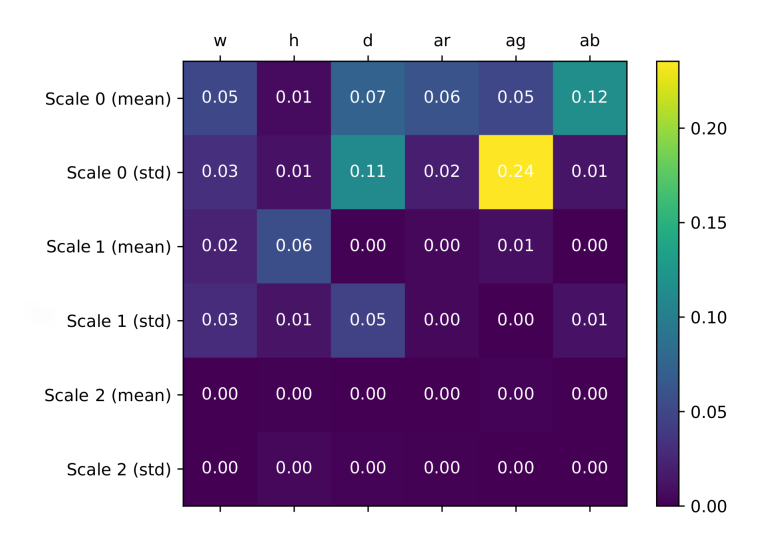


Figure 8: The importance of each of 36 attributes averaged over 15 decision trees obtained with ASR.

allows forming compact, informative and explainable representations, which are not only capable of conveying the essence of the content of the input image, but also constructing potent predictors with high explanatory power.

ASR offers natural means for providing a learning system with domain knowledge in the form of the repertoire of visual primitives. For the class of images considered in this study, elliptical shapes proved sufficient to outperform a conventional DL baseline. It is likely, however, that more sophisticated graphical representations could further improve the quality of reconstruction and the accuracy of the resulting classifiers; for instance, the Fourier-based shape representations used in [Krawiec and Nowinowski, 2024] offer more flexibility in shape modeling, and thus could likely convey more relevant information. For this and other domains, whether involving medical imaging or not, there is no shortage of types of visual primitives that be selected to match their characteristics. Moreover, the potential applications of this approach extend beyond the visual domain, as the only prerequisite of the method is the availability of primitives that can be parameterized and 'rendered' in a differentiable fashion.

Acknowledgments

This research was supported by the statutory funds of Poznan University of Technology and the Polish Ministry of Science and Higher Education, grants no. 0311/SBAD/0740 and 0311/SBAD/0752.

The data

Table 3 provides the detailed information about the dataset created for this study.

Table 3: The 30 digital slides from the BRD database Bio [2023] of GTEx images used in this study. These examinations were selected using the search keyword "Thyroid gland". Each entry contains the image in SVS format and metadata, including the case ID, sex, and age (presented below). Another field in the database contains pathology review comments, for instance, "2 pieces, no abnormalities". This global information was used to determine the class of the sample (seen in the Class column). In total, ten images per class were selected – five for training, two for validation. and three for testing. The last column describes the number of patches extracted from a digital slide.

Case ID	Class	Sex	Age	URL	Subset	Patches
GTEX-1128S	Benign	Female	61-70	https://brd.nci.nih.gov/brd/specimen/GTEX-1128S-0126	train	1171
GTEX-1192X	Benign	Male	51-60	https://brd.nci.nih.gov/brd/specimen/GTEX-1192X-1126	train	1246
GTEX-12KS4	Benign	Male	21-40	https://brd.nci.nih.gov/brd/specimen/GTEX-12KS4-0526	train	500
GTEX-13NYB	Benign	Male	41-50	https://brd.nci.nih.gov/brd/specimen/GTEX-13NYB-0726	train	774
GTEX-13PL6	Benign	Female	41-50	https://brd.nci.nih.gov/brd/specimen/GTEX-13PL6-1026	train	679
GTEX-13QBU	Benign	Female	21-40	https://brd.nci.nih.gov/brd/specimen/GTEX-13QBU-0626	val	993
GTEX-1A8G6	Benign	Male	61-70	https://brd.nci.nih.gov/brd/specimen/GTEX-1A8G6-0626	val	1252
GTEX-1AMFI	Benign	Female	51-60	https://brd.nci.nih.gov/brd/specimen/GTEX-1AMFI-0526	test	177
GTEX-14DAR	Benign	Male	41-50	https://brd.nci.nih.gov/brd/specimen/GTEX-14DAR-0126	test	715
GTEX-1F5PL	Benign	Female	41-50	https://brd.nci.nih.gov/brd/specimen/GTEX-1F5PL-0826	test	580
Total	_					8087
GTEX-14PJ6	Hashimoto	Female	61-70	https://brd.nci.nih.gov/brd/specimen/GTEX-14PJ6-0326	train	493
GTEX-14PJM	Hashimoto	Female	51-60	https://brd.nci.nih.gov/brd/specimen/GTEX-14PJM-1326	train	694
GTEX-XBEC	Hashimoto	Male	51-60	https://brd.nci.nih.gov/brd/specimen/GTEX-XBEC-0926	train	745
GTEX-1AX8Y	Hashimoto	Male	41-50	https://brd.nci.nih.gov/brd/specimen/GTEX-1AX8Y-0126	train	757
GTEX-14BMU	Hashimoto	Female	21-40	https://brd.nci.nih.gov/brd/specimen/GTEX-14BMU-0226	train	845
GTEX-1C6WA	Hashimoto	Male	61-70	https://brd.nci.nih.gov/brd/specimen/GTEX-1C6WA-0626	test	868
GTEX-11XUK	Hashimoto	Female	41-50	https://brd.nci.nih.gov/brd/specimen/GTEX-11XUK-0226	test	729
GTEX-YJ8A	Hashimoto	Male	21-40	https://brd.nci.nih.gov/brd/specimen/GTEX-YJ8A-0226	test	1 549
GTEX-13QJC	Hashimoto	Female	61-70	https://brd.nci.nih.gov/brd/specimen/GTEX-13QJC-0826	val	565
GTEX-WVJS	Hashimoto	Male	51-60	https://brd.nci.nih.gov/brd/specimen/GTEX-WVJS-0726	val	1 055
Total						8300
GTEX-1MCYP	Nodularity	Female	21-40	https://brd.nci.nih.gov/brd/specimen/GTEX-1MCYP-0626	train	444
GTEX-1KD5A	Nodularity	Male	51-60	https://brd.nci.nih.gov/brd/specimen/GTEX-1KD5A-0426	train	900
GTEX-15DCD	Nodularity	Female	61-70	https://brd.nci.nih.gov/brd/specimen/GTEX-15DCD-1126	train	574
GTEX-111GQ	Nodularity	Male	51-60	https://brd.nci.nih.gov/brd/specimen/GTEX-1I1GQ-0826	train	624
GTEX-131XW	Nodularity	Female	51-60	https://brd.nci.nih.gov/brd/specimen/GTEX-131XW-0826	train	469
GTEX-18QFQ	Nodularity	Male	21-40	https://brd.nci.nih.gov/brd/specimen/GTEX-18QFQ-0726	val	429
GTEX-13SLX	Nodularity	Female	51-60	https://brd.nci.nih.gov/brd/specimen/GTEX-13SLX-0726	val	651
GTEX-11EQ8	Nodularity	Male	61-70	https://brd.nci.nih.gov/brd/specimen/GTEX-11EQ8-0826	test	976
GTEX-130VJ	Nodularity	Female	51-60	https://brd.nci.nih.gov/brd/specimen/GTEX-130VJ-0626	test	709
GTEX-11TUW	Nodularity	Male	61-70	https://brd.nci.nih.gov/brd/specimen/GTEX-11TUW-0226	test	932
Total	•					6708

Configurations and hyperparameter settings

The following parameters shared the same settings across all architectures considered in this study:

Optimizer: The Adam optimizer Kingma and Ba [2017] has been used as it become the default choice in many deep learning frameworks due to its solid generalization performance across a wide range of tasks.

Learning Rate = 0.001: A starting point in many deep learning tasks. Across the experiments, several other values were tested, however, the initially used learning rate equal to 0.001 turned out to work the best for our case.

Batch Size = 32: A default value that is often chosen for memory efficiency, especially when training on GPUs.

Number of batches per epoch = 32: In most deep learning approaches, an *epoch* refers to one complete cycle through the training data. However, in our implementation, it was decided to control the number of batches, and hence images processed by the learning algorithm in each iteration. Such a defined mechanism allowed the evaluation of the model performance more often. As a result, in one epoch $32 \times 32 = 1024$ images were passed through the model (the total size of the training set is 10,915 images).

Number of epochs = 50 (55 for some configurations): The maximum training duration for the model to show the convergence. In the configuration with the freezing of layers, it was decided to increase the number of epochs to 55.

Table 4: Weight initialization method by component and layer.

Component	Layer	Weights	Bias
ConvBlock	Conv2d	Xavier	Normal
Modeler	Conv2d	Xavier	Normal
BackgroundBlock	Linear	Xavier	Ones

- Loss Function: The Masked Mean Squared Error (MMSE) function described in Section 2.2 was used to not force the model to generate shapes that are only partially present in the input image.
- Early Stopping: A default PyTorch EarlyStopping handler with patience = 20 was used to terminate the training if no improvement concerning the validation loss was seen after 20 epochs. It allowed us to reduce the computational costs and speed up the experimental process.
- Weight Initialization: Xavier weight initialization Glorot and Bengio [2010] has been used as it is a widely recommended choice for many neural network architectures, and more importantly, to prevent the vanishing gradient problem. See Table 4 for initialization details per component.
- Seed: To make different configurations more comparable, a fixed seed was set in PyTorch. It ensured that between particular training configurations, the order of the training data passed through the model, as well as the initial weights of the model, were the same.
- Data Augmentation: While the built-in PyTorch module for image augmentation was initially incorporated as an optional training feature, offering support for vertical or horizontal flipping and rotating images at 90/180/270 degrees, it has been deactivated in all configurations due to a sufficient amount of data.

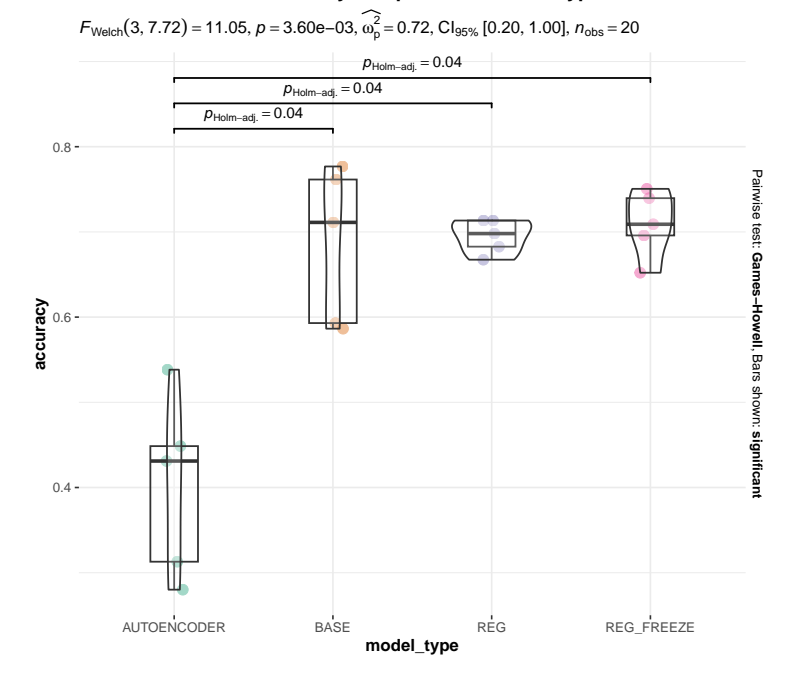
Statistical testing of classification results

We conducted statistical tests (Fig. 9), which confirm that our encoder-modeler-renderer models are better than the autoencoders on accuracy and weighed average of F1-score.

References

- Nikhila Ravi, Jeremy Reizenstein, David Novotny, Taylor Gordon, Wan-Yen Lo, Justin Johnson, and Georgia Gkioxari. Accelerating 3d deep learning with pytorch3d. (arXiv:2007.08501), 2020. doi:10.48550/arXiv.2007.08501.
- Tzu-Mao Li, Michal Lukáč, Gharbi Michaël, and Jonathan Ragan-Kelley. Differentiable vector graphics rasterization for editing and learning. ACM Trans. Graph. (Proc. SIGGRAPH Asia), 39(6):193:1–193:15, 2020.
- Clement Fuji Tsang, Maria Shugrina, Jean Francois Lafleche, Towaki Takikawa, Jiehan Wang, Charles Loop, Wenzheng Chen, Krishna Murthy Jatavallabhula, Edward Smith, Artem Rozantsev, Or Perel, Tianchang Shen, Jun Gao, Sanja Fidler, Gavriel State, Jason Gorski, Tommy Xiang, Jianing Li, Michael Li, and Rev Lebaredian. Kaolin: A pytorch library for accelerating 3d deep learning research. https://github.com/NVIDIAGameWorks/kaolin, 2022.
- Wenzel Jakob, Sébastien Speierer, Nicolas Roussel, Merlin Nimier-David, Delio Vicini, Tizian Zeltner, Baptiste Nicolet, Miguel Crespo, Vincent Leroy, and Ziyi Zhang. Mitsuba 3 renderer, 2022. https://mitsuba-renderer.org.
- Xavier Glorot and Yoshua Bengio. Understanding the difficulty of training deep feedforward neural networks. In Yee Whye Teh and Mike Titterington, editors, Proceedings of the Thirteenth International Conference on Artificial Intelligence and Statistics, volume 9 of Proceedings of Machine Learning Research, pages 249–256, Chia Laguna Resort, Sardinia, Italy, 13-15 May 2010. PMLR. URL https://proceedings.mlr.press/v9/glorot10a.
- Harry Barrow, J Tenenbaum, A Hanson, and E Riseman. Recovering intrinsic scene characteristics. *Comput. vis. syst*, 2 (3-26):2, 1978.
- Krzysztof Krawiec. Generative learning of visual concepts using multiobjective genetic programming. Pattern Recogn. Lett., 28(16):2385–2400, dec 2007. ISSN 0167-8655. doi:10.1016/j.patrec.2007.08.001.
- Jinyang Yuan, Tonglin Chen, Bin Li, and Xiangyang Xue. Compositional scene representation learning via reconstruction: A survey. IEEE Transactions on Pattern Analysis and Machine Intelligence, 45(10):11540-11560, 2023. doi:10.1109/TPAMI.2023.3286184.

Parametric test for accuracy comparison between types of models



Parametric test for F1 score comparison between types of models

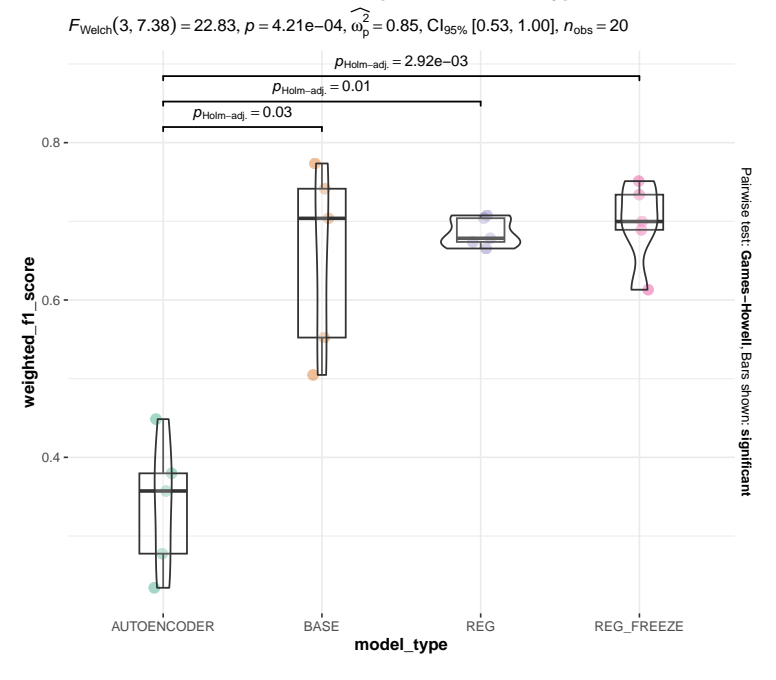


Figure 9: Results of the one-way ANOVA and the post-hoc tests for accuracy (top) and F1-score (bottom). A model is a composition of encoder-modeler and the best decision tree classifier. The normality of residuals was confirmed using the Shapiro-Wilk tests. Low *p*-values indicate that at least one type of models is significantly different in terms of performance. The Games-Howell post-hoc tests revealed significant differences between the Baseline ('AUTOENCODER') and all remaining architectures.

Cathrin Elich, Martin R. Oswald, Marc Pollefeys, and Joerg Stueckler. Weakly supervised learning of multi-object 3d scene decompositions using deep shape priors. *Computer Vision and Image Understanding*, 220:103440, 2022.

- ISSN 1077-3142. doi:10.1016/j.cviu.2022.103440.
- Christopher P. Burgess, Loic Matthey, Nicholas Watters, Rishabh Kabra, Irina Higgins, Matt Botvinick, and Alexander Lerchner. Monet: Unsupervised scene decomposition and representation. (arXiv:1901.11390), January 2019. doi:10.48550/arXiv.1901.11390.
- Wei-Chih Hung, Varun Jampani, Sifei Liu, Pavlo Molchanov, Ming-Hsuan Yang, and Jan Kautz. Scops: Self-supervised co-part segmentation. In 2019 IEEE/CVF Conference on Computer Vision and Pattern Recognition (CVPR), pages 869–878, 2019. doi:10.1109/CVPR.2019.00096.
- Subhabrata Choudhury, Iro Laina, Christian Rupprecht, and Andrea Vedaldi. Unsupervised part discovery from contrastive reconstruction. In M. Ranzato, A. Beygelzimer, Y. Dauphin, P.S. Liang, and J. Wortman Vaughan, editors, *Advances in Neural Information Processing Systems*, volume 34, pages 28104–28118. Curran Associates, Inc., 2021.
- Krzysztof Krawiec and Antoni Nowinowski. Disentangling visual priors: Unsupervised learning of scene interpretations with compositional autoencoder. In Tarek R. Besold, Artur d'Avila Garcez, Ernesto Jimenez-Ruiz, Roberto Confalonieri, Pranava Madhyastha, and Benedikt Wagner, editors, *Neural-Symbolic Learning and Reasoning*, pages 240–256, Cham, 2024. Springer Nature Switzerland. ISBN 978-3-031-71167-1.
- Biospecimen research database. http://biospecimens.cancer.gov/brd, 2023. URL http://biospecimens.cancer.gov/brd. Accessed: 07.12.2023.
- Andrew Janowczyk. Converting an existing image into an openslide compatible format, Dec 2020. URL http://www.andrewjanowczyk.com/converting-an-existing-image-into-an-openslide-compatible-format/.
- Zhou Wang, Alan Conrad Bovik, Hamid Rahim Sheikh, and Eero P Simoncelli. Image quality assessment: from error visibility to structural similarity. *IEEE Trans. Image Process.*, 13(4):600–612, April 2004.
- F. Pedregosa, G. Varoquaux, A. Gramfort, V. Michel, B. Thirion, O. Grisel, M. Blondel, P. Prettenhofer, R. Weiss, V. Dubourg, J. Vanderplas, A. Passos, D. Cournapeau, M. Brucher, M. Perrot, and E. Duchesnay. Scikit-learn: Machine learning in Python. *Journal of Machine Learning Research*, 12:2825–2830, 2011.
- L. Breiman, Jerome H. Friedman, Richard A. Olshen, and C. J. Stone. Classification and regression trees. *Biometrics*, 40:874, 1984. URL https://api.semanticscholar.org/CorpusID:29458883.
- Diederik P. Kingma and Jimmy Ba. Adam: A method for stochastic optimization, 2017.